2018-07-01

Synchronization of the astronomical time scales in the Early Toarcian: a link between anoxia, carbon-cycle perturbation, mass extinction and volcanism

Ait-Itto, F-Z

10.1016/j.epsl.2018.04.007
Earth and Planetary Science Letters
Elsevier

Synchronization of the astronomical time scales in the Early Toarcian: a link between anoxia, carbon-cycle perturbation, mass extinction and volcanism

Fatima-Zahra Ait-Itto [a,*], Mathieu Martinez [b,c], Gregory D. Price [d], Abdellah Ait Addi [a]

[a] Cadi Ayyad University, Faculty of Sciences and Techniques, Geosciences and Environmental research's Laboratory, P.O. Box 549, Marrakech, Morocco

[b] MARUM: Center for Marine Environmental Sciences, Universität Bremen, Leobenerstr., 28359 Bremen, Germany.

[c] Univ Rennes, CNRS, Géosciences Rennes - UMR 6118, 35000 Rennes, France

[d] School of Geography, Earth and Environmental Sciences Plymouth University, Plymouth, Devon PL4 8AA, UK

Abstract

The Late Pliensbachian-Early Toarcian is a pivotal time in the Mesozoic era, marked by pronounced carbon-isotope excursions, biotic crises and major climatic and oceanographic changes. Here we present new high-resolution carbon-isotope and magnetic-susceptibility measurements from an expanded hemipelagic Late Pliensbachian-Early Toarcian section from the Middle Atlas Basin (Morocco). Our new astronomical calibration allows the construction of an orbital time scale based on the 100-kyr eccentricity cycle. The Early Toarcian Polymorphum Zone contains 10 to 10.5 repetitions of the 100-kyr eccentricity both in the carbon-isotope and the magnetic-susceptibility data, leading to an average duration of 1.00 ± 0.08 myr. We also show that the Late Pliensbachian-Early Toarcian global carbon-cycle perturbation has an average duration of 0.24 ± 0.02 myr. These durations are comparable to previous astrochronological time scales provided for this time interval in the most complete

sections of the Tethyan area, and longer than what has been provided in condensed sections. Anchoring this framework on published radiometric ages and astrochronological time scales, we estimate that the carbon-cycle perturbation of the Late Pliensbachian-Early Toarcian corresponds with the early phase of the Karoo and Chonke Aike large igneous provinces. Likewise, our new age constraints confirm that the Toarcian oceanic anoxic event is synchronous to the main phase of the Ferrar volcanic activity. Thus, these successive and short phases of the volcanic activity may have been at the origin of the successive phases of the mass extinctions observed in marine biotas in the Pliensbachian and Toarcian times.

Keywords:

Astrochronology; Toarcian; carbon cycle; Middle Atlas; oceanic anoxic events

1. Introduction

The Early Toarcian (184.15 – 174.1 Ma) was a time of global warming events (Dera et al., 2011), mass extinctions (Little and Benton, 1995), and pronounced negative carbon-isotope excursions recorded in marine carbonates and organic matter, brachiopods, biomarkers and fossil wood (Hesselbo et al., 2007; Suan et al., 2008a; Ait-Itto et al., 2017). These events coincide with carbonate production demises (Bassoullet and Baudin, 1994; Wilmsen and Neuweiler, 2008) and widespread oceanic anoxia (Jenkyns, 1988; Hesselbo et al., 2007).

Although large amounts of data have been produced, the timing and rhythms of the environmental perturbations are still debated, leading to controversies on the mechanisms at the onset of the climatic changes in the Early Toarcian (e.g. Kemp et al., 2005; Suan et al., 2008b). For instance, Martinez et al (2017) assess the duration of Pliensbachian-Toarcian event (P-To event) at 0.18 to 0.27 myr, while in the Peniche section (Lusitanian Basin, Portugal) the duration of this event is evaluated as 0.05 myr (Suan et al., 2008b). Similarly, the estimates of duration of the Polymorphum Zone vary from 90 kyr to 1.15 myr (Matiolli and Pittet, 2004; Suan et al.,

2008b, Boulila et al., 2014; Huang and Hesselbo, 2014; Ruebsam et al., 2014; Martinez et al., 2017). The main reason of these differences is the occurrence of four discontinuity events identified by correlations of $\delta^{13}C$ and sedimentological features throughout the Tethyan margins, which are due to changes in the sea level observed in the earliest Toarcian (Pittet et al., 2014). The section studied here in Issouka, Morocco, is expanded compared to the sedimentary series from the northern Tethyan margin. It provides the opportunity to fill the gap in the time scale of the Toarcian Stage and to establish a detailed chronology of the succession of the environmental disturbances occurring in the Early Toarcian.

2. Geological setting

The geological history of Morocco was influenced by two important events, starting in the early Mesozoic with the opening of the north Atlantic and western Tethys and the collision of Africa and Europe during the middle Cenozoic (Michard, 1976). These events led to the formation of fault-bounded basins, which are made up of several smaller depocenters, separated by synsedimentary highs (Studer and Du Dresnay, 1980). The Middle Atlas is one of these small fault-bounded basins (Fig. 1). It constitutes a part of a Meso-Cenozoic intracontinental chain, namely the Moroccan Atlas (Michard, 1976). The Middle Atlas of Morocco is structurally dominated by four NE–SW trending anticlines and is mainly constituted of Lower and Middle Jurassic formations (Du Dresnay, 1971). The basin is bounded by the Saïs Plain and the front of the Rifian Nappes in the North, by the Guercif Basin in the northeast, by the Moulouya Plain to the southeast, and by the Hercynian Central Massif in the West.

The Middle Atlas Basin is deep in the center and shallows towards the northern and southern basin margins (Du Dresnay, 1971). The study area during the Early Toarcian was located at a palaeolatitude of ~20°N (Bassoulet et al., 1993) (Fig. 1A). The sedimentary evolution and palaeogeographic differentiation is controlled by tectonic activity, combined with

the rate of sedimentation and global eustatic variations (Wilmsen and Neuweiler, 2008). The rapid transition from shallow marine carbonates to hemipelagic marls has been taken to reflect a major deepening phase across the entire Middle and High Atlas area (Wilmsen and Neuweiler, 2008). The Pliensbachian–Toarcian transition coincides with a dislocation of the Lower Jurassic carbonate platform (Lachkar et al., 2009; Ait Addi and Chafiki, 2013) with Toarcian deposits dominated by marls lying upon Upper Pliensbachian shallow marine limestones and calcareous marls. This drowning episode is linked to the eustatic sea-level rise of the Early Toarcian described in Europe and Africa (e.g. Hallam, 1997).

The biostratigraphy in the Middle Atlas has been established with ammonites (El Hammichi et al., 2008) with further biostratigraphic data provided by benthic foraminifera (Bejjaji et al., 2010). The ammonite zonation in the Issouka section is based on the Mediterranean zonation. Notably, the ammonites *Emaciaticeras emaciatum* of the Emaciatum Zone, *Dactylioceras polymorphum* of the Toarcian Polymorphum Zone and *Hildaites* in the Semicelatum Zone have been identified (e.g. El Hammichi et al., 2008). Furthermore, the occurrence of the benthic foraminifera *Lenticulina sublaevis* in the Issouka section is correlated by Bejjaji et al. (2010) to the Emaciatum ammonite zone of the Pliensbachian, whilst *Lenticulina bochardi* and *Lenticulina toarcense* are correlated with the Toarcian Polymorphum Zone and *Lenticulina obonensis* with the Serpentinus Zone.

The Issouka section is situated near the village of Issouka, ~25 km southwest of Immouzer Marmoucha, in the Middle Atlas (N33° 26’ 55.56”; W4° 20’ 33.83”; Fig. 1). The section begins with centimeter thick limestone–marl alternations (Fig. 2). The limestone beds contain a rich ammonite fauna, with also belemnites, echinoids and brachiopods. Foraminifera suggested a Late Pliensbachian age (Bejjaji et al., 2010; Fig. 2A). The early Toarcian succession starts with green marls and marl–limestone alternations, rich in foraminifera, belemnites,

echinoids and gastropods. The Toarcian deposits are generally hemipelagic and correspond to deep marine environments (Bejjaji et al., 2010; Fig. 2B).

3. Material and methods

A total of 430 bulk-rock samples were collected with an even sample distance of 10 cm in the Issouka section. The samples were recovered from up to 15 cm below the surface, to minimize the effects of surface weathering. The sampled interval encompasses the end of the Pliensbachian Stage to the lowermost part of the Levisoni ammonite Zone. Such a range allows the Polymorphum Zone to be entirely sampled. The bulk-rock samples were then powdered using a metal ring grinder and analyzed for stables isotopes, magnetic susceptibility and calcium carbonate contents.

3.1. Carbon isotopes

A total of 430 samples were analyzed for stable isotopes at the University of Plymouth. Using 200 to 300 micrograms of carbonate, stable isotope data were generated on a VG Optima mass spectrometer with a Gilson autosampler. Isotope ratios were calibrated using NBS19 standards and are given in δ notation relative to the Vienna Pee Dee Belemnite (VPDB). Reproducibility was generally better than 0.1 ‰ for samples and standard material.

3.2. Magnetic susceptibility

The magnetic susceptibility (MS) of the 430 powdered samples was measured with a Kappabridge KLY-3. The samples are placed in small plastic cubes of 10 cm^3 and then introduced inside the instrument using the “pick-up” unit. We measured the cube empty and then with samples for blank correction. The blank-corrected MS values are normalized to their mass and volume. The resulting values are reported as mass-specific MS ($m^3.kg^{-1}$).

3.3. Calcium carbonate content

The samples were analyzed for their calcium carbonate content using a Bernard calcimeter at the Geosciences and Environment Laboratory, Cadi Ayyad University. The values are given with a precision between 1 and 5% (Lamas et al., 2005).

3.4. Spectral analysis

Prior to spectral analysis, the long-term trend of both series was measured and subtracted from the series to ensure stationarity. The detrend procedures removed the high powers in the frequencies close to 0, while not creating new spectral peaks in the low frequencies (see Vaughan et al., 2015). Best-fit linear trend and LOWESS smoothing curves (Cleveland et al., 1979) were applied. The exact coefficients depend on each of the series and are detailed in the results. Following the removal of this long-term trend, the multi-taper spectral analyses, using three 2π prolate tapers (2π-MTM) with robust red-noise modelling (Mann and Lees, 1996) modified in Meyers (2014) were applied to evaluate lithological cycles as a possible record of astronomically forced sedimentation following the LOWSPEC approach (Meyers, 2012). The significance levels were then calculated assuming a chi-square distribution of the spectral background. We used the time-frequency weighted fast Fourier transforms (T-F WFFT; Martinez et al., 2015) to characterize the evolution of the periods through the sedimentary series. Taner low-pass and band-pass filters (Taner, 2003) were then applied to isolate each signal interpreted as an orbital forcing and calculate the duration of the Polymorphum Zone by cycle counting. Orbital tuning procedures are then used to anchor the sedimentary cycles to their corresponding orbital periods, allowing depth-time conversions to be done. Durations are then estimated by calculating the difference of relative ages. Error margins of each of the time

intervals include the difference between the average and the calculated durations and the uncertainty in the orbital frequencies.

4. Results

4.1. Carbonate carbon isotopes

The carbon-isotope profile of the Issouka section shows relatively high values in the Pliensbachian part of the section, ranging from +1.7‰ to +2.7‰ (Fig. 3A). From 5 m to 5.6 m, the $\delta^{13}C$ decreases from 2.5‰ to -0.6‰. This abrupt decrease of 3‰ in the $\delta^{13}C$ observed at the base of the Toarcian is related to the Pliensbachian-Toarcian event (P-To event; Suan et al., 2008a; Ait-Itto et al., 2017). The $\delta^{13}C$ values then remain low from 5 m to 23 m. In this interval, the values show gentle fluctuations from 5 to 17 m. At 17 m, the $\delta^{13}C$ abruptly increase by 1‰ before they gently decrease until 23 m to -2‰. The values then progressively increase from 23 m to 30 m, changing from -2‰ to 1‰. Above 30 m to the top of the section, the values slightly increase from 1 to 2‰.

4.2. Magnetic susceptibility

The magnetic susceptibility curve (Fig. 3E) firstly shows from the base of the series to level 5.1 m low values, ranging from 9.65×10^{-9} to 3.15×10^{-8} $m^3.kg^{-1}$. This interval corresponds to the limestone-dominated part of the formation of Pliensbachian age. From 5.2 m to the top of the series, MS values increase with an average value 1.04×10^{-7} $m^3.kg^{-1}$. The interval from 27 m to 35 m shows lower values of the MS in a more carbonated interval. Calcium carbonate content and MS values display a strong inverse correlation (r = -0.91, Fig. 4), indicating that the lithology mainly controls the MS variations.

4.3. Calcium carbonate content

The carbonate content series (Fig. 3D) firstly show high values (>80% on average) from the base of the series to 5.1 m, in the interval of the limestone beds of the Pliensbachian. From 5.2

m to 8.4 m, the values rapidly decrease from 91% to 8.6%. From 5.2 m to 18 m, the $CaCO_3$ values remain low with average values around 22%. The transition between the first to the second interval is more progressive than observed in the $\delta^{13}C$ series (Fig. 3A). From 18 m to 42.9 m $CaCO_3$ series show high-amplitude cycles and high-frequency fluctuations from 60% and 20% linked to the limestone-marl alternations (Fig. 3D).

4.4. Spectral analyses

4.4.1. Carbon-isotope signal

The $\delta^{13}C$ shows a rapid decrease at 5.2 m, and a rapid increase at 16.6 m (Fig. 3A). The series was stationarized using a best-fit linear trend from 0 to 5.1 m, a LOWESS regression with a coefficient of 0.6 from 5.2 to 16.5 m and a LOWESS regression with a coefficient of 0.3 from 16.6 to 42.9 m. The LOWESS coefficients have been chosen in such a way that they approximatively cover the same length of the section (i.e. ~7 m on average), which represents *ca.* 20% of the Toarcian part. This choice decreased the high powers at frequencies near 0, while not creating spurious spectral peaks in the low frequencies (Vaughan et al., 2015). The three subseries were then standardized (average = 0, standard deviation = 1) and stacked. Two points at 11.7 m and 12 m showing outstandingly low values when detrending may bias the spectrum in the high frequencies and have been removed from the series before detrending. The evolutive spectrum of the $\delta^{13}C$ series shows a high-power spectral band in the low frequencies evolving having a period of 4.1 to 4.2 m from the base of the series to level 24 m (Fig. 3C). The period of this band then decreases to 3 m, from level 24 m to level 31 m, and stabilizes at 3 m from level 31 m to the top of the series. These changes in the period of the ~4-m peak likely reflects variations in the sedimentation rate. These distort the sedimentary record of the orbital cycles by decreasing the *p*-value of the low frequency and flattening the spectrum at high frequencies (Weedon, 2003; Kemp, 2016; Martinez et al., 2016). We thus decided to analyze the frequency content of two sub-intervals of the series in which variations in the sedimentation

rate are limited. The range of each of the sub-intervals is given in Fig. 3C. We compared the frequencies of the carbon isotopes in each interval with the orbital frequencies calculated for the Toarcian (Waltham, 2015), using the average spectral misfit (ASM; Meyers and Sageman, 2007). The ASM method compares the sedimentary frequencies converted into time to the orbital frequencies and provides a quantitative assessment on the most likely sedimentation rate in each sub-interval (see supplementary materials).

Spectra of Interval 1, from levels 0 to 31 m, show significant periods above the 99% confidence level (CL) at 4.2 m (frequency: 0.2404 cycles.m^{-1}), and above the 95% CL at 1.2 m (frequency: 0.8013 cycles.m^{-1}), 0.83 m (frequency: 1.202 cycles.m^{-1}), and 0.31 m (Fig. 5A, C). Spectra of Interval 2, from levels 24 m to the top of the series show significant peaks above the 95% CL at 3.2 m (frequency: 0.3158 cycles.m^{-1}), 0.63 m (1.579 cycles.m^{-1}) and 0.33 m (Fig. 5B, D).

As noted above, various astrochronological frameworks estimate the duration of the Polymorphum Zone from 0.09 myr to 1.15 myr (Mattioli and Pittet, 2004; Suan et al., 2008b; Huang and Hesselbo, 2014; Boulila et al., 2014; Martinez et al., 2017; Boulila and Hinnov, 2017), implying a sedimentation rate varying from 400 m/myr to 31 m/myr. When converting m-cycles to time-cycles, the peaks at ~0.3 m have periods below the Milankovitch band whatever the sedimentation rate considered, so were excluded from the ASM analysis. Testing ASM over 500 sedimentation rates ranging from 0.4 cm/kyr to 40 cm/kyr leads to a most likely sedimentation rate of 3.9 cm/kyr (39 m/myr) in Interval 1, and to a most likely sedimentation rate of 3.2 cm/kyr (32 m/myr) in Interval 2 (Fig. 5E, F). The H0-significance level at the most likely sedimentation rate is below the critical significance level below which we can consider without ambiguity these spectra reflect an orbital forcing. In Interval 1, peaks at 4.2 m, 1.2 m and 0.83 m are respectively due to the 100-kyr eccentricity, the obliquity and the precession cycles. Notice than the peak of 1.2 m leads to an obliquity period which is shorter than expected

224 in the theory (here 29.4 kyr vs. 37.5 kyr in Waltham, 2015). In Interval 2, peaks at 3.2 m and
225 0.63 m are respectively due to the 100-kyr eccentricity and the precession cycles. In addition,
226 the peak at 0.33 m has a mean period of 10 kyr, which corresponds to the semi-precession, the
227 first harmonic of the precession (Berger et al., 2006).

228 The evolutive spectral analysis indicates the 100-kyr cycle is the most continuous
229 throughout the studied series (Fig. 3C). We filtered the 100-kyr eccentricity recorded in the
230 $\delta^{13}C$ series and used it as target cycle for calibrating the series in time. We filtered the 100-kyr
231 cycle using a Taner low-pass filter with a frequency cut of 0.3953 cycles.m^{-1} and a roll-off rate
232 of 10^{36}. The output filter indicates that the Polymorphum Zone contains 10 repetitions of the
233 100-kyr eccentricity cycle (Fig. 3B).

234

235 **4.4.2. Magnetic susceptibility**

236 The MS series is marked by a rapid increase of values from 5.0 m to 6.8 m. The trend of the
237 series is then gentler. The series was stationarized using a best-fit linear regression from 0 to
238 5.2 m and a LOWESS smoothing with a coefficient of 0.2 in the remainder of the series, which
239 represents 7.5 m of the section. The two subseries were then standardized (average = 0, standard
240 deviation = 1) and stacked. The evolutive spectrum of the MS series shows a band in the low
241 frequencies evolving from 3.1 m to 3.7 m in the lower part of the series, from the base of the
242 series to level 20 m (Fig. 3G). Then, this period decreases to 2.9 m from level 26 m to the top
243 of the series. 2π-MTM spectra have been generated from Interval 1 (from the base of the series
244 to level 26 m), and from Interval 2 (from 21 m to the top of the series) (Fig. 6). Spectra of
245 Interval 1 show spectral peaks over the 99% CL at 3.3 m and 0.38 m, and peaks over the 95%
246 CL at 0.81 m and 0.23 m (Fig. 6A, C). Spectra of Interval 2 show peaks over the 99% CL at 2.9
247 m, 2.0 m, 0.27 m and 0.22 m, and a peak exceeding the 95% CL at 1.0 m (Fig. 6B, D).

248 Assuming from ASM applied on the $\delta^{13}C$ spectra that Interval 1 has a mean
249 sedimentation rate of 39 m/myr, the peaks of 3.3 m, 0.81 m and 0.38 m are attributed to the
250 100-kyr eccentricity, the precession and the semi-precession, respectively. Assuming from
251 ASM that Interval 2 has a mean sedimentation rate of 32 m/myr, the peak of 2.9 m, 1.0 m and
252 0.27 m are respectively attributed to the 100-kyr eccentricity, the obliquity and the semi-
253 precession (Fig. 6).

254 In Interval 1, the period of the 100-kyr cycle is lower in the MS series than in the $\delta^{13}C$.
255 On the evolutive spectral analyses, this is particularly obvious in the first 10 m of the series,
256 when the lithology evolves from the limestones of the Pliensbachian to the marls of the Toarcian
257 (Fig. 3). The 100-kyr eccentricity recorded in the MS series was isolated using a Taner low-
258 pass filter with a frequency cut of 0.4070 cycles.m^{-1} and a roll-off rate of 10^{36} (Fig. 3). The
259 output filter indicates that the Polymorphum Zone clearly contains ~10.5 repetitions of the 100-
260 kyr eccentricity cycle compared to the 10 repetitions observed in the $\delta^{13}C$ (Fig. 3).

261

262 **5. Discussion**

263 **5.1. Astrochronology of the the Polymorphum Zone**

264 The $\delta^{13}C$ and the MS signals both display 12 complete short eccentricity cycles along the
265 studied section. In the astronomical models computed for the last 20 myr (Laskar et al., 2004),
266 the average duration of 12 consecutive short eccentricity cycles is 1149 ± 63 kyr (2σ), so that
267 the average duration of a short eccentricity cycle 95.8 ± 5.2 kyr (2σ). Assuming a constant
268 sedimentation rate between two successive anchor points of the 100-kyr cycle obtained from
269 the filters of the $\delta^{13}C$ and the MS signals, the durations calculated of the Polymorphum Zone
270 range from 0.97 myr with the $\delta^{13}C$ signal, to 1.02 myr with the MS signal. In the spectra of the
271 untuned series, the period of the 100-kyr cycle is longer in the $\delta^{13}C$ than in the MS (Figs. 3, 5,
272 6). The difference is particularly noticeable in the first 10 m (Fig. 3). Below level 5 m, the filter

of 100-kyr cycle in the $\delta^{13}C$ is inversely correlated to the filter of the 100-kyr in the MS signal. After 5 m, i.e. after the start of the P-To event, the two filters are in phase. The limestone beds in the Pliensbachian of the atlasic basins originate from exports from the neritic environments, in which the $\delta^{13}C$ was higher than in pelagic environments (Wilmsen and Neuweiler, 2008). In the Pliensbachian, the $\delta^{13}C$ is higher in limestone beds. The P-To Event corresponds to a demise in the neritic carbonate production. Fluctuations in the $\delta^{13}C$ thus correspond to fluctuations in the pelagic production, which is usually higher during the deposit of marlier intervals, when detrital and nutrient increased the primary productivity (Mutterlose and Ruffell, 1999; Mattioli and Pittet, 2004). The demise of the carbonate platforms thus changed the phasing between the MS and the $\delta^{13}C$, which is a source of uncertainty in the calculation of the durations. Another change of phasing occurs at 28 m, where the $\delta^{13}C$ and the $CaCO_3$ content increase. As the phasing between the orbital configuration and the proxies is still unclear, we choose to retain the average duration of 1.00 ± 0.08 myr for the Polymorphum Zone (the uncertainty includes the age model and the duration of a short eccentricity period, see supplementary materials).

The spectrum of the calibrated $\delta^{13}C$ shows a high power at 96 kyr (expected when calibrated to the short eccentricity), 32.4 kyr (main obliquity), 24.1 and 19.7 kyr (precession), and 13.2 to 11.0 kyr (half-precession) (Fig. 7A). In addition, a peak exceeding the 95% confidence level appears at 400 kyr, which corresponds to the long-eccentricity cycle. The spectrum of the calibrated MS shows a high power at 95.7 kyr (expected), 65.5 kyr, 31.9 kyr (main obliquity), from 24.4 to 19.1 kyr (precession), and from 12.1 to 10.6 kyr (half precession) (Fig. 7B). In the $\delta^{13}C$ and MS signals, the precession cycle has slightly longer periods than expected in the theory (Waltham, 2015). This may be the consequence of a precession cycle missing per short eccentricity. In the astronomical solutions, the amplitude of the precession band is modulated by the 405-kyr and the 100-kyr eccentricity cycles, while the amplitude of the 100-kyr cycle is modulated by the 400-kyr cycle (Laskar et al., 2004). The Taner band-pass

filter of the precession cycle in the $\delta^{13}C$ series was performed with frequency cuts of 3.583 x 10^{-2} cycles/kyr and 5.417 x 10^{-2} cycles/kyr, and a roll-off rate of 10^{36} (Fig. 8B, E). We calculated the amplitude modulation (AM) of the precession cycles using a Hilbert transform. The spectrum of the AM of the precession filter shows cycles at 340 kyr (near the 405-kyr eccentricity), and at 123 and 82.8 kyr (near the periods of 124 and 95 kyr of the short eccentricity) (Fig. 8F). We filtered the 100-kyr band of the AM of the precession filter using a Taner band-pass filter with frequency cuts of 6.250 x 10^{-3} cycles/kyr and 1.558 x 10^{-2} cycles/kyr and a roll-off rate of 10^{36} (Fig. 8F). The AM of this filter shows a cycle at 340 kyr (Fig. 8G). Similarly, the spectrum of the AM calculated on the direct filter of the 100-kyr band shows a cycle at 436 kyr (Fig. 8H). Thus, the AM of the precession and the 100-kyr eccentricity show similar patterns as expected in the astronomical models. The filters of the two bands shows 11 cycles of short eccentricity within the Polymorphum Zone (Fig. 8C), while the various filters of the 405-kyr cycles in the AM of the precession and the 100-kyr cycles show from 3 to 4 repetitions of the 405-kyr cycle (Fig. 8A, C, D). The difference between the direct filter and the filter of the AM is explained by the residence time of carbon in the ocean, which creates a delay in the response of the $\delta^{13}C$ to the orbital forcing (Laurin et al., 2017). In this context of hemipelagic sediments, with the limestone beds originating from exports from neritic environments, the difference may also be due to the change of the carbonate source.

The duration of the Polymorphum Zone from this study is longer than the duration of ~0.8 myr assessed in the Peniche section (Suan et al., 2008b; Huang and Hesselbo, 2014) and the Foum Tillicht section (Martinez et al., 2017). The correlation of these sections led to a duration of a composite Polymorphum Zone of 0.9-1.0 myr, which agrees with the duration calculated here. In addition, the duration calculated here is in close agreement with the duration estimated from Central Italy, in which 11 bundles of marl-limestone alternations have been related to the 100-kyr eccentricity cycle (Mattioli and Pittet, 2004).

323 The series of condensation affecting the Pliensbachian-Toarcian transition strongly
324 affects the duration assessments in the Northern Tethyan margin. For instance, in the Paris
325 Basin, the duration of the Tenuicostatum Zone (equivalent to Polymorphum) varies from 0.09
326 myr to 0.5 myr (Boulila et al., 2014; Ruebsam et al., 2014). Correlations of $\delta^{13}C$ curves indicate
327 that these sections are affected by a series of condensation events, leading to an underestimation
328 of the duration of the Tenuicostatum Zone (Pittet et al., 2014). Recently, Boulila and Hinnov
329 (2017) suggested that the 100-kyr eccentricity cycles identified in Suan et al. (2008b) and
330 Huang and Hesselbo (2014) are the record of the obliquity cycle. However, this would imply a
331 hiatus of ~800 kyr in the middle of the Tenuicostatum Zone, which is not indicated in the $\delta^{13}C$
332 data (Pittet et al., 2014). In addition, detailed observations of the sedimentological pattern of
333 Peniche indicate than these cycles correspond to bundles of 4-6 marl-limestone alternations,
334 which is related to the hierarchy in between the short eccentricity and precession (Suan et al.,
335 2008b). We thus retain here for the Peniche section the astrochronological models from Suan
336 et al. (2008b) and Huang and Hesselbo (2014).
337
338 **5.2 Duration of the P-To Event**
339 The duration of the P-To event varies from ~50 kyr to 0.27 myr from various astrochronological
340 models (Suan et al., 2008b; Huang and Hesselbo, 2014; Martinez et al., 2017). Uncertainties
341 are due to the condensation event often observed at the Pliensbachian-Toarcian boundary (Pittet
342 et al., 2014) and to the difficulty in defining the upper boundary of the P-To event (Martinez et
343 al., 2017). The P-To event indeed starts with an abrupt decrease of 2 to 3‰ the $\delta^{13}C$ and change
344 in lithology from carbonated to detrital sediment (Suan et al., 2008a; Bodin et al., 2010). Then,
345 the $\delta^{13}C$ values gently increase, making the definition of an upper limit of the P-To event
346 problematic. Martinez et al. (2017) defined two options to define the upper boundary of the P-
347 To event: (i) the end of the decrease of the $\delta^{13}C$ and $CaCO_3$ values; (ii) the local increase of the

348 $\delta^{13}C$ values in the lower part of the Polymorphum Zone, corresponding to a maximum of the
349 filter of the 405-kyr band in the $\delta^{13}C$. In the Issouka section, the filter of the 405-kyr band was
350 calculated on the calibrated series (high frequency cut: 0.005833 cycles/kyr; roll-off rate: 10^{36})
351 and converted into depths shows that this maximum is at 13.1 m (Fig. 9). We suggest using this
352 marker as the end of the P-To event, as it can be observed both in the Central High Atlas and
353 the Middle Atlas. From the $\delta^{13}C$ and the MS age models, the duration of the P-To event as
354 defined here varies from 0.23 to 0.25 myr, with an average duration of 0.24 ± 0.02 myr (this
355 uncertainty takes into account the uncertainty of the age model and the uncertainty of the period
356 of the eccentricity, see supplementary materials). These durations are in agreement with Option
357 1 from the Foum Tillicht section, which vary from 0.25 to 0.29 myr, with an average duration
358 of 0.27 myr (Martinez et al., 2017). This duration of the P-To event appears stable in Moroccan
359 sections, ranging from 0.23 to 0.29 myr.
360
361 **5.3. A synthetic astrochronology for the Tethyan area in the Early Toarcian**
362 The Polymorphum Zone at Issouka shows 10 to 10.5 repetitions of the 100-kyr eccentricity
363 cycles. In comparison, the sedimentary records of Foum Tillicht and Peniche show a total of
364 eight 100-kyr eccentricity cycles for the Polymorphum Zone. Lithological patterns in the
365 Umbria-Marche Basin tend to indicate that the Polymorphum Zone contains ten to eleven
366 repetitions of 100-kyr cycle (Mattioli and Pittet, 2004). Four discontinuities identified in the
367 Pliensbachian-Toarcian transition have affected the completeness of the sedimentary record in
368 the Foum Tillicht and the Peniche sections. In particular, at Peniche, the Pliensbachian-Toarcian
369 transition appears condensed, while in Foum Tillicht the top of Polymorphum is missing
370 (Martinez et al., 2017). In Issouka, Foum Tillicht and Peniche, $\delta^{13}C$ has been measured at a
371 high resolution and astrochronologies have been produced, making it possible to correlate the
372 sections at a Milankovitch scale.

373 Based on the astrochronological frameworks produced in this study and in Huang and
374 Hesselbo (2014) and Martinez et al. (2017), we can correlate these three sections at the
375 eccentricity scale (Fig. 9). Radiometric ages have been anchored on stratigraphic ages at the
376 Triassic-Jurassic boundary, in the Hettangian and the Sinemurian (Ruhl et al., 2016). A U-Pb
377 age has been proposed for the uppermost part of the Tenuicostatum Zone at 183.22 ± 0.26 Ma
378 in Southern Peru (Sell et al., 2014). The lack of intercalibration with astrochronology makes it
379 difficult to anchor it on our time scale. Conversely, the Triassic-Jurassic boundary have been
380 bracketed at 201.36 ± 0.17 Ma with U-Pb ages from the Pucara Basin (Peru) and the New York
381 Canyon (Nevada, USA), recalibrated applying version 3.0 of EARTHTIME tracer (Wotzlaw et
382 al., 2014). The duration of the interval from the base of the Jurassic to the base of the Toarcian
383 have been assessed at 17.21 myr (Ikeda and Tada, 2014), which matches with the time scale
384 suggested in Ruhl et al. (2016) with an uncertainty of ± one 405-kyr cycle. It positions the base
385 of the Toarcian at 184.15 ± 0.58 Ma. The uncertainty retained here corresponds to the sum of
386 uncertainties of astrochronology and radiochronology.
387 Other ages are as follows (see also supplementary materials for details of the
388 calculations):
389 - The average duration of the P-To event is 0.24 ± 0.02 myr, positioning the top of the P-To
390 event at 183.91 ± 0.60 myr,
391 - The average duration of the Tenuicostatum/Polymorphum Zone is 1.00 ± 0.08 myr,
392 positioning the top of Tenuicostatum/Polymorphum at 183.15 ± 0.66 Ma. Notice that this age
393 fits with the age of Sell et al. (2014) of 183.22 ± 0.26 Ma for the uppermost part of the
394 Tenuicostatum Zone,
395 - The base of the T-OAE occurs 0.03 myr after the end of the Polymorphum Zone (Huang and
396 Hesselbo, 2014; Fig. 9), i.e. 183.12 ± 0.66 Ma,

- The T-OAE encompasses 11 short-eccentricity cycles (Suan et al., 2008b; Huang and Hesselbo, 2014; Thibault et al., 2018), corresponding to a duration of 1.05 ± 0.06 myr (Fig. 9). The top of the T-OAE is thus dated here at 182.07 ± 0.72 Ma,

5.4. Origins of P-To and T-OAE disturbances

The large negative CIEs observed in the Early Toarcian, the P-To event and the T-OAE, imply the injection of large amount of light carbon in the oceanic system (Suan et al., 2015). This has been interpreted as dissociation of methane hydrate, maybe orbitally paced (Kemp et al., 2005), or production of thermogenic methane due to volcanic intrusion during the Karoo-Ferrar activity (Svensen et al., 2007). The long duration of the T-OAE (Suan et al., 2008b; Huang and Hesselbo, 2014) implies that the amount of methane needed to maintain the negative excursion for such a long time would exceed the volume of gas hydrate reservoir (Suan et al., 2008b). In addition, the interval of the T-OAE display a positive excursion in Hg/TOC, associated with a volcanic activity (Percival et al., 2015). CA-ID-TIMS U-Pb ages indicate that the Ferrar province activity occurred from 182.779 ± 0.033 Ma and lasted 349 ± 49 kyr (Burgess et al., 2015). These ages fall in the range of the ages assessed here for the T-OAE (183.12 ± 0.66 Ma to 182.07 ± 0.72 Ma; Fig. 9). All these observations tend to favour the crucial role of the Karoo-Ferrar activity on the inception of the T-OAE. Hg/TOC data from Yorkshire and the Peniche sections show a positive excursion within the P-To event, which tend to indicate the concomitance between the P-To event and volcanic activity. The P-To event started 184.15 ± 0.58 Ma and ended at 183.91 ± 0.60 Ma (Fig. 9), so that the P-To event appears significantly older than the activity of the Ferrar province. Dating of the early phase of the Karoo province tends to indicate that the Karoo province started earlier than the Ferrar (Burgess et al., 2015; Moulin et al., 2017). Notably the oldest $^{40}Ar/^{39}Ar$ ages of the Karoo activity have been found in the southern part of the Barkly East Formation (South Africa), within the Omega and the

Moshesh's Ford units (Moulin et al., 2017 and references therein). Other ages older than 183 Ma have been reported in the Northern part of the Chonke Aike LIP (South America) in the Rio Negro Province and in the eastern part of the Chubut Province (Féraud et al., 1999). The location and the thicknesses of the formations in which these older $^{40}Ar/^{39}Ar$ and and U/Pb ages have been provided are, to our knowledge, much more limited than that of the main phase of the Karoo-Ferrar activity (~183 Ma). While this main phase is likely to be responsible for the inception of the T-OAE, limited volcanic activities in the early phase of the Karoo and Chonke Aike LIP may have affected the environmental and ecological perturbations recorded at the Pliensbachian-Toarcian boundary.

6. Conclusions

The carbon isotope and MS variations in the Late Pliensbachian-Early Toarcian, performed in the expanded hemipelagic in Issouka section from the Middle Atlas Basin, Morocco, reveal superposed frequencies consistent with Milankovitch forcing (eccentricity, obliquity, and precession). The Polymorphum Zone contains 10 to 10.5 repetitions of the 100-kyr eccentricity cycle, so that its duration is assessed here at 1.00 ± 0.08 myr. The duration of the P-To event is in addition assessed at 0.24 ± 0.02 myr. The recognition of the 100-kyr and the 405-kyr eccentricity enabled us to establish a stratigraphic framework between the Northern and the Southern Tethyan margins. Anchoring this framework on published radiometric ages and astrochronological time scales, we could estimate the age of the base of the Toarcian as 184.15 ± 0.58 Ma, the top of the P-To event as 183.91 ± 0.60 Ma, the base of the Toarcian OAE as 183.12 ± 0.66 Ma, and the top of the Toarcian OAE as 182.07 ± 0.72 Ma. The age of the Toarcian OAE fits with the ages published for the Ferrar volcanic activity. Conversely, the age of the P-To event seems to correspond with early phase of the Karoo and Chonke Aike activity. Thus, the successive and short phases of the volcanic activity of the Chonke Aike, Karoo and

Ferrar provinces may have been the smoking gun of the successive phases of the mass extinction observed in marine biotas in the Pliensbachian and Toarcian times.

Acknowledgements

This paper benefitted considerably from 3 constructive reviews. We would like to thank also the IAS Postgraduate Grant Scheme for the financial support that Fatima-Zahra Ait-Itto received in 2016 for making the isotopic analyses at Plymouth University. Mathieu Martinez was supported by ERC Consolidator Grant Earthsequencing.

References

Ait Addi, A., Chafiki, D., 2013. Sedimentary evolution and palaeogeography of mid Jurassic deposits of the Central High Atlas, Morocco. J. Afr. Earth Sci. 84, 54–69. https://doi.org/10.1016/j.jafrearsci.2013.04.002.

Ait-Itto, F.-Z., Price, G.D., Ait Addi, A., Chafiki, D., Mannani, I., 2017. Bulk-carbonate and belemnite carbon-isotope records across the Pliensbachian-Toarcian boundary on the northern margin of Gondwana (Issouka, Middle Atlas, Morocco). Palaeogeogr. Palaeoclim. Palaeoecol. 466, 128–136. https://doi.org/10.1016/j.palaeo.2016.11.014.

Bassoullet, J.P., Baudin, F., 1994. Le Toarcien inférieur : une période de crise dans les bassins et sur les plate-formes carbonatées de l'Europe du Nord-Ouest et de la Téthys. Geobios. 17, 645–654. https://doi.org/10.1016/S0016-6995(94)80227-0.

Bassoulet, J., Elmi, S., Poisson, F., Cecca, F., Belion, Y., Guiraud, R., Baudin, F., 1993. Mid Toarcian. In: Dercourt, J., Ricou, L.E., Vrielynck, B. (Eds.), Atlas Tethys, Paleoenvironmental Maps: Becip–Franlab, Rueil–Malmaison, France, 63–80.

Bejjaji, Z., Chakiri, S., Reolid, M., Boutakiout, M., 2010. Foraminiferal biostratigraphy of the Toarcian deposits (Lower Jurassic) from the Middle Atlas (Morocco). Comparison with

472 western Tethyan areas. J. Afr. Earth Sci. 57, 154–162.
473 https://doi.org/10.1016/j.jafrearsci.2009.08.002.
474 Berger, A., Loutre, M.F., Melice, J.L., 2006. Equatorial insolation: from precession harmonics
475 to eccentricity frequencies. Clim. Past 2, 131–136. https://doi.org/10.5194/cp-2-131-
476 2006.
477 Bodin, S., Mattioli, E., Fröhlich, S., Marshall, J.D., Boutib, L., Lahsini, S., Redfern, J., 2010.
478 Toarcian carbon isotope shifts and nutrient changes from the Northern margin of
479 Gondwana (High Atlas, Morocco, Jurassic): Palaeoenvironmental implications.
480 Palaeogeogr. Palaeocl. 297, 377–390. https://doi.org/10.1016/j.palaeo.2010.08.018.
481 Boulila, S., Galbrun, B., Huret, E., Hinnov, L.A., Rouget, I., Gardin, S., Bartolini, A., 2014.
482 Astronomical calibration of the Toarcian Stage: Implications for sequence stratigraphy
483 and duration of the early Toarcian OAE. Earth and Planet. Sci. Lett. 386, 98–111.
484 https://doi.org/10.1016/j.epsl.2013.10.047.
485 Boulila, S., Hinnov L.A., 2017. A review of tempo and scale of the early Jurassic Toarcian
486 OAE: implications for carbon cycle and sea level variations. Newsl. Stratigr. In press.
487 https://doi.org/10.1127/nos/2017/0374.
488 Burgess, S.D., Bowring, S.A., Fleming, T.H., Elliot, D.H., 2015. High-precision geochronology
489 links the Ferrar large igneous province with early-Jurassic ocean anoxia and biotic crisis.
490 Earth Planet. Sci. Lett. 415, 90–99. https://doi.org/10.1016/j.epsl.2015.01.037.
491 Cleveland, W.S., 1979. Robust Locally Weighted Regression and Smoothing Scatterplots.
492 Journal of the American Statistical Association 74, 829-836.
493 Dera, G., Brigaud, B., Monna, F., Laffont R., Pucéat, E., Deconinck, J.-F., Pellenard, P.,
494 Joachimski, M.M., Durlet, C., 2011. Climatic ups and downs in a disturbed Jurassic
495 world. Geology 39, 215–218. http://dx.doi.org/10.1130/G31579.1.

Du Dresnay, R., 1971. Extension et développement des phénomènes récifaux Jurassique dans le domaine Atlasique Marocain, particulièrement au Lias moyen. Bull. Soc. Geol. Fr. 13, 46–56. http://dx.doi.org/10.2113/gssgfbull.S7-XIII.1-2.46.

El Hammichi, F., Benshili, K., Elmi, S., 2008. Les faunes d'Ammonites du Toarcien-Aalénien du Moyen Atlas sud-occidental (Maroc). Rev. Paléobiol. 27, 429–447.

Féraud, G., Alric, V., Fornari, M., Bertrand, H., Haller, M., 1999. 40Ar/39Ar dating of the Jurassic volcanic province of Patagonia: migrating magmatism related to Gondwana break-up and subduction. Earth Planet. Sci. Lett. 172, 83–96. https://doi.org/10.1016/S0012-821X(99)00190-9.

Hallam, A., 1997. Estimates of the amount and rate of the of sea level change across the Rhaetian–Hettangian and Pliensbachian–Toarcian boundary (latest Triassic to Early Jurassic). J. Geol. Soc. Lond. 154, 773–779. http://dx.doi.org/10.1144/gsjgs.154.5.0773.

Hesselbo, S.P., Jenkyns, H.C., Duarte, L.V., Oliveira, L.C.V., 2007. Carbon–isotope record of the Early Jurassic (Toarcian) Oceanic Anoxic Event from fossil wood and marine carbonate (Lusitanian Basin, Portugal). Earth Planet. Sci. Lett. 253, 455–470. https://doi.org/10.1016/j.epsl.2006.11.009.

Huang, C., Hesselbo, S.P., 2014. Pacing of the Toarcian Oceanic Anoxic Event (Early Jurassic) from astronomical correlation of marine sections. Gondwana Res. 25, 1348–1356. https://doi.org/10.1016/j.gr.2013.06.023.

Ikeda, M., Tada, R., 2014. A 70 million year astronomical time scale for the deep-sea bedded chert sequence (Inuyama, Japan): Implications for Triassic–Jurassic geochronology. Earth Planet. Sci. Lett. 399, 30–43. https://doi.org/10.1016/j.epsl.2014.04.031.

Jenkyns, H.C., 1988. The Early Toarcian anoxic event: stratigraphic, sedimentary and geochemical evidence. Am. J. Sci. 288, 101–151.

521 Kemp, D.B., Coe, A.L., Cohen, A.S., Schwark, L., 2005. Astronomical pacing of methane
522 release in the Early Jurassic period. Nature 437, 396–399.
523 http://dx.doi.org/10.1038/nature04037.
524 Lachkar, N., Guiraud, M., El Harfi, A., Dommergues, J. L., Dera, G., Durlet, C., 2009. Early
525 Jurassic normal faulting in a carbonate extensional basin: characterization of
526 tectonically driven platform drowning (High Atlas rift, Morocco). J. Geol. Soc. Lond.
527 166, 413–430. http://dx.doi.org/10.1144/0016-76492008-084.
528 Lamas, F., Irigaray, C., Oteo, C., Chacón, J., 2005. Selection of the most appropriate method
529 to determine the carbonate content for engineering purposes with particular regard to
530 marls. Eng. Geol. 81, 32–41. https://doi.org/10.1016/j.enggeo.2005.07.005.
531 Laskar, J., Robutel, P., Joutel, F., Gastineau, M., Correia, A.C.M., Levrard, M., 2004. A long-
532 term numerical solution for the insolation quantities of the Earth. Astronom. Astrophys.
533 428, 261-285. https://doi.org/10.1051/0004-6361:20041335.
534 Laurin, J., Růžek, B., Giorgioni, M., 2017. Orbital Signals in Carbon Isotopes: Phase Distortion
535 as a Signature of the Carbon Cycle. Paleoceanography 32, 1236–1255.
536 http://dx.doi.org/10.1002/2017PA003143.
537 Little, C.T.S., Benton, M.J., 1995. Early Jurassic mass extinction: a global long–term event.
538 Geology 23, 495–498.
539 http://dx.doi.org/10.1130/0091-7613(1995)023<0495:EJMEAG>2.3.CO;2.
540 Littler, K., Hesselbo, S.P., Jenkyns, H.C., 2010. A carbon-isotope perturbation at the
541 Pliensbachian–Toarcian boundary: evidence from the Lias Group, NE England.
542 Geological Magazine 147, 181–192. https://doi.org/10.1017/S0016756809990458.
543 Kemp, D.B., 2016. Optimizing significance testing of astronomical forcing in
544 cyclostratigraphy. Paleoceanography 31, https://doi.org/10.1002/2016PA002963.

Mann, M.E., Lees, J.M., 1996. Robust estimation of background noise and signal detection in climatic time series. Climatic Change 33, 409–445. http://dx.doi.org/10.1007/BF00142586.

Martinez, M., Deconinck, J.-F., Pellenard, P., Riquier, L., Company, M., Reboulet, S., Moiroud, M., 2015. Astrochronology of the Valanginian-Hauterivian stages (Early Cretaceous): chronological relationships between the Paraná–Etendeka large igneous province, the Weissert and the Faraoni events. Global Planet. Change 131, 158–173. https://doi.org/10.1016/j.gloplacha.2015.06.001.

Martinez, M., Kotov, S., De Vleeschouwer, D., Pas, D., Pälike, H., 2016. Testing the impact of stratigraphic uncertainty on spectral analyses of sedimentary series. Clim. Past 12, 1765–1783. https://doi.org/10.5194/cp-12-1765-2016.

Martinez, M., Krencker, F.N., Mattioli E., Bodin, S., 2017. Orbital chronology of the Pliensbachian–Toarcian transition from the Central High Atlas Basin (Morocco). Newsletters on Stratigraphy 50, 47–69. https://doi.org/10.1127/nos/2016/0311.

Mattioli, E., Pittet, B., 2004. Spatial and temporal distribution of calcareous nannofossils along a proximal–distal transect in the Lower Jurassic of the Umbria–Marche Basin (central Italy). Palaeogeogr. Palaeoclim. Palaeoecol. 205, 295–316. https://doi.org/10.1016/j.palaeo.2003.12.013.

Meyers, S.R., Sageman, B.B., 2007. Quantification of deep-time orbital forcing by average spectral misfit. Am. J. Sci. 307, 773–792. http://dx.doi.org/10.2475/05.2007.01.

Meyers, S.R., 2012. Seeing red in cyclic stratigraphy: Spectral noise estimation for astrochronology. Paleoceanography 27, PA 3228. http://dx.doi.org/10.1029/2012PA002307.

Meyers, S.R., 2014. Astrochron: An R Package for Astrochronology. [Available at http://cran.r-project.org/package=astrochron.]

570 Michard, A., 1976. Eléments de géologie Marocaine. Notes et Mémoires du Service Géologique
571 252, 408.
572 Moulin, M., Fluteau, F., Courtillot, V., Marsh. J., Delpech, G., Quidelleur, X., and Gérard, M.,
573 2017. Eruptive history of the Karoo lava flows and their impact on early Jurassic
574 environmental change. J. Geophys. Res. Solid Earth. 122, 738–772.
575 http://dx.doi.org/10.1029/2011JB008210.
576 Mutterlose, J., Ruffell, A., 1999. Milankovtich-scale palaeoclimate changes in pale–dark
577 bedding rhythms from the Early Cretaceous (Hauterivian and Barremian) of eastern
578 England and northern Germany. Palaeogeogr. Palaeoclim. Palaeoecol. 154, 133–160.
579 https://doi.org/10.1016/S0031-0182(99)00107-8.
580 Percival, L.M.E., Witt, M.L.I., Mather, T.A., Hermoso, M., Jenkyns, H.C., Hesselbo, S.P., Al-
581 Suwaidi, A.H., Storm, M.S., Xu, W., Ruhl, M., 2015. Globally enhanced mercury
582 deposition during the end-Pliensbachian extinction and Toarcian OAE: a link to the
583 Karoo–Ferrar Large Igneous Province. Earth Planet. Sci. Lett. 428, 267–280.
584 https://doi.org/10.1016/j.epsl.2015.06.064.
585 Pittet, B., Suan, G., Lenoir, F., Duarte, L.V., Mattioli E., 2014. Carbon isotope evidence for
586 sedimentary discontinuities in the lower Toarcian of the Lusitanian Basin (Portugal):
587 Sea level change at the onset of the Oceanic Anoxic Event. Sediment. Geol. 303, 1–14.
588 https://doi.org/10.1016/j.sedgeo.2014.01.001.
589 Ruebsam, W., Münzberger, P. and Schwark, L., 2014. Chronology of the Early Toarcian
590 environmental crisis in the Lorraine Sub-Basin (NE Paris Basin). Earth Planet. Sci. Lett.
591 404, 273–282. https://doi.org/10.1016/j.epsl.2014.08.005.
592 Ruhl, M., Hesselbo, S.P., Hinnov, L., Jenkyns, H.C., Xu, W., Riding, J.B., Storm, M., Minisini,
593 D., Ullmann,C.V., Leng, M.J., 2016. Astronomical constraints on the duration of the

Early Jurassic Pliensbachian Stage and global climatic fluctuations. Earth Planet. Sci. Lett. 455, 149–165. https://doi.org/10.1016/j.epsl.2016.08.038.

Sell, B., Ovtcharova, M., Guex, J., Bartolini, A., Jourdan, F., Spangenberg, J.E., Vicente, J., Schaltegger, U., 2014. Evaluating the temporal link between the Karoo LIP and climatic–biologic events of the Toarcian Stage with high-precision U–Pb geochronology. Earth Planet. Sci. Lett. 408, 48–56. https://doi.org/10.1016/j.epsl.2014.10.008.

Studer, M., Du Dresnay, R., 1980. Déformations synsédimentaires en compression pendant le Lias supérieur et le Dogger, au Tizi n'lrhil (Haut Atlas central de Midelt, Maroc). Bull. Soc. Geol. Fr. 22, 391–397. http://dx.doi.org/10.2113/gssgfbull.S7-XXII.3.391.

Suan, G., Mattioli, E., Pittet, B., Mailliot, S. and Lécuyer, C., 2008a. Evidence for major environmental perturbation prior to and during the Toarcian (Early Jurassic) oceanic anoxic event from the Lusitanian Basin, Portugal. Paleoceanography. 23, PA1202. http://dx.doi.org/10.1029/2007PA001459.

Suan, G., Pittet, B., Bour, I., Mattioli, E., Duarte, L. and Mailliot, S., 2008b. Duration of the Early Toarcian carbon isotope excursion deduced from spectral analysis: Consequence for its possible causes. Earth Planet. Sci. Lett. 267, 666–679. https://doi.org/10.1016/j.epsl.2007.12.017.

Suan, G., van de Schootbrugge, B., Adatte, T., Fiebig, J., Oschmann, W., 2015. Calibrating the magnitude of the Toarcian carbon cycle perturbation. Paleoceanography. 30, PA002758. http://dx.doi.org/10.1002/2014PA002758.

Svensen, H., Planke, S., Chevallier, L., Malthe-Sorenssen, A., Corfu, F., Jamtveit, B., 2007. Hydrothermal venting of greenhouse gases triggering Early Jurassic global warming. Earth Planet. Sci. Lett. 256, 554–566. https://doi.org/10.1016/j.epsl.2007.02.013.

618 Taner, M.T., 2003. Attributes Revisited, Technical Publication. Rock Solid Images, Inc.,
619 Houston, TX (URL: rocksolidimages.com/pdf/attrib_revisited.htm.).
620 Thibault, N., Rhul, M., Ullmann, C.V., Korte, C., Kemp, D.B., Gröcke, D.R., Hesselbo, S.P.,
621 2018. The wider context of the Lower Jurassic Toarcian oceanic anoxic event in
622 Yorkshire coastal outcrops, UK. Proceedings of the Geologists' Association, in press.
623 https://doi.org/10.1016/j.pgeola.2017.10.007.
624 Vaughan, S., Bailey, R.J., Smith, D.G., 2015. Cyclostratigraphy: data filtering as a source of
625 spurious spectral peaks. Geological Society, London, Special Publications 404, 151-
626 156. https://doi.org/10.1144/SP404.11.
627 Weedon, G.P., 2003. Time-Series Analysis and Cyclostratigraphy: Examining stratigraphic
628 records of environmental cycles. Cambridge University Press, Cambridge.
629 Waltham. D., 2015. Milankovitch Period Uncertainties and Their Impact on Cyclostratigraphy.
630 J. Sediment. Res. 85, 990–998. http://dx.doi.org/10.2110/jsr.2015.66.
631 Wilmsen, M. and Neuweiler, F., 2008. Biosedimentology of the Early Jurassic post-extinction
632 carbonate depositional system, central High Atlas rift basin, Morocco. Sedimentology
633 55, 773–807. http://dx.doi.org/10.1111/j.1365-3091.2007.00921.x.
634 Wotzlaw, J.-F., Guex, J., Bartolini, A., Gallet, Y., Krystyn, L., McRoberts, C.A., Taylor, D.,
635 Schoene, B., Schaltegger, U., 2014. Towards accurate numerical calibration of the Late
636 Triassic: high-precision U–Pb geochronology constraints on the duration of the
637 Rhaetian. Geology. 42, 571–574. http://dx.doi.org/10.1130/G35612.1.
638

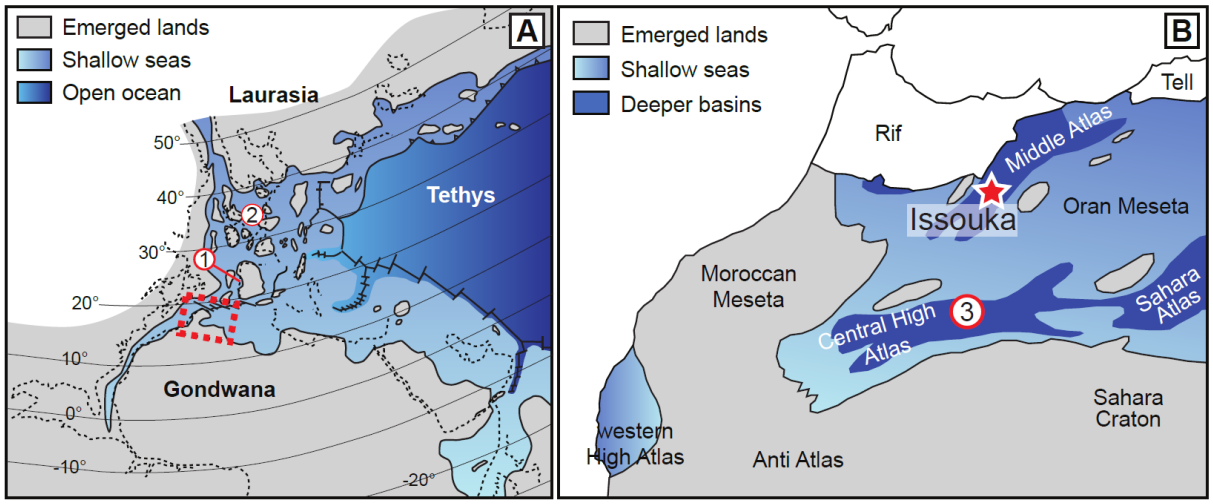

639

640

641 Fig. 1. Geological setting of the Issouka section. **A.** Palaeogeographic map of the western Tethys during
642 the Early Jurassic. The red dash rectangle shows the limit of the second map. Label "1" indicates the
643 location of the Peniche section. Label "2" indicates the location of Yorkshire area. **B.** Geographical map
644 of Morocco and western Algeria showing the main geological provinces and the location of the Issouka
645 section within the Middle Atlas. Label "3" indicates the location of the Foum Tillicht section (maps
646 from Bodin et al., 2010).

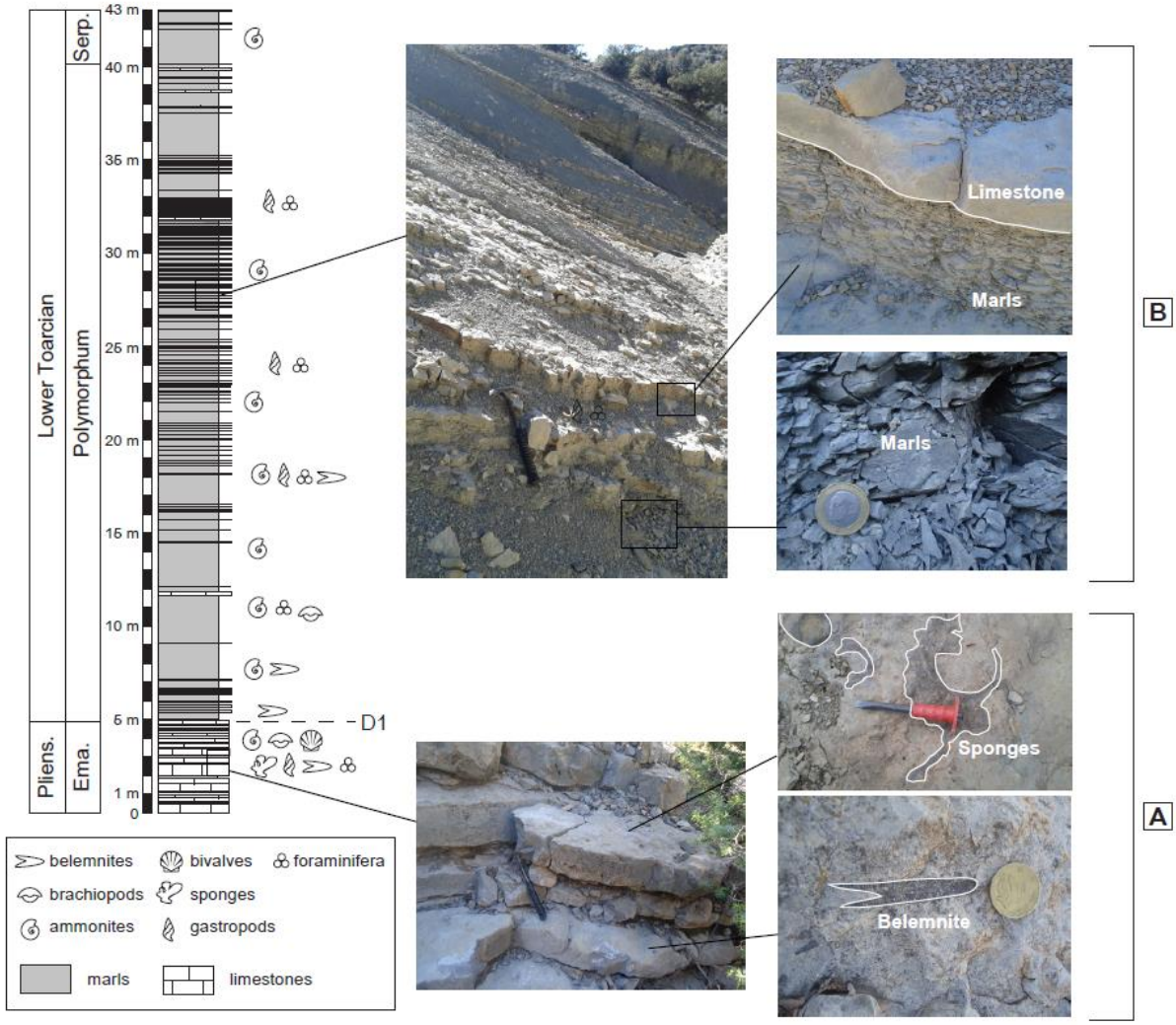

Fig. 2. The different facies in the Issouka section. **A.** Limestone of the late Pliensbachian with fauna (belemnites, sponges and brachiopods). **B.** The Lower Toarcian, characterized by grey marls and limestone intercalations.

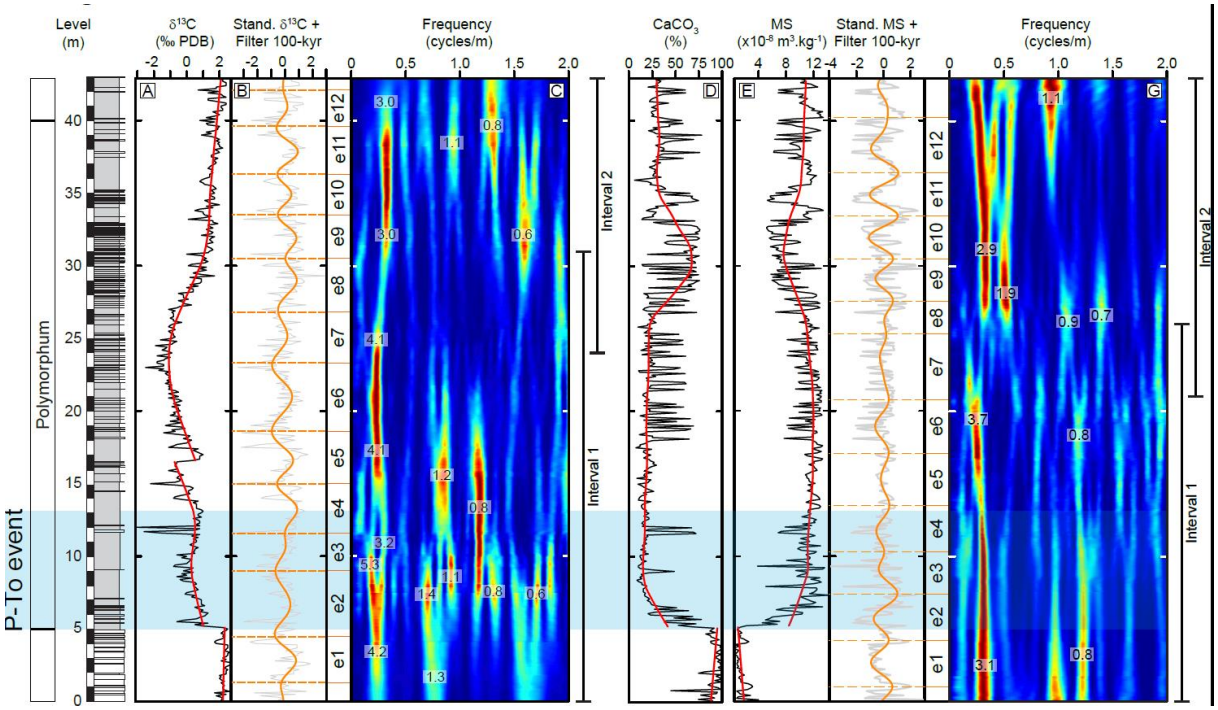

Fig. 3. Raw data, spectrograms and filters of the 100-kyr eccentricity band of the carbon isotope ($\delta^{13}C$) and magnetic susceptibility (MS) signals. **A.** Raw $\delta^{13}C$ signal (in black) with long-term trend (in red). **B.** Standardised $\delta^{13}C$ signal (in grey) with the filter of the 100-kyr eccentricity (in orange). **C.** Spectrogram of the $\delta^{13}C$ signal performed with 15-m-width windows. **D.** Raw $CaCO_3$ signal (in black) with long-term trend (in red). **E.** Raw MS signal (in black) with long-term trend (in red). **F.** Standardised MS signal (in grey) with the filter of the 100-kyr eccentricity (in orange). **G.** Spectrogram of the MS signal performed with 15-m-width windows.

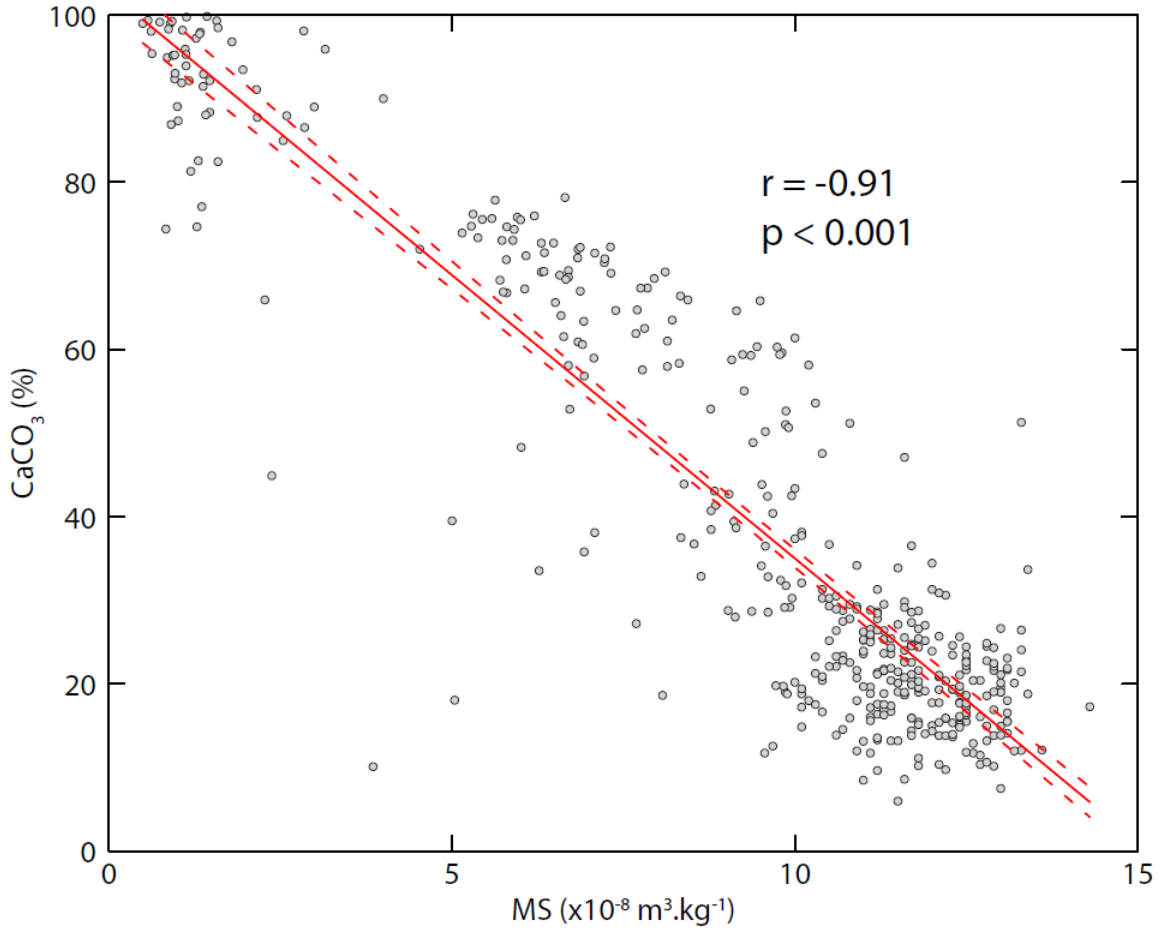

Fig. 4. Cross-plot of the magnetic susceptibility (MS) versus calcium carbonate content ($CaCO_3$). The full red line is the best-fit linear regression, while dash lines are the 95% confidence intervals of the linear regression. *r* indicates the coefficient correlation, and *p* is the *p*-value of the correlation.

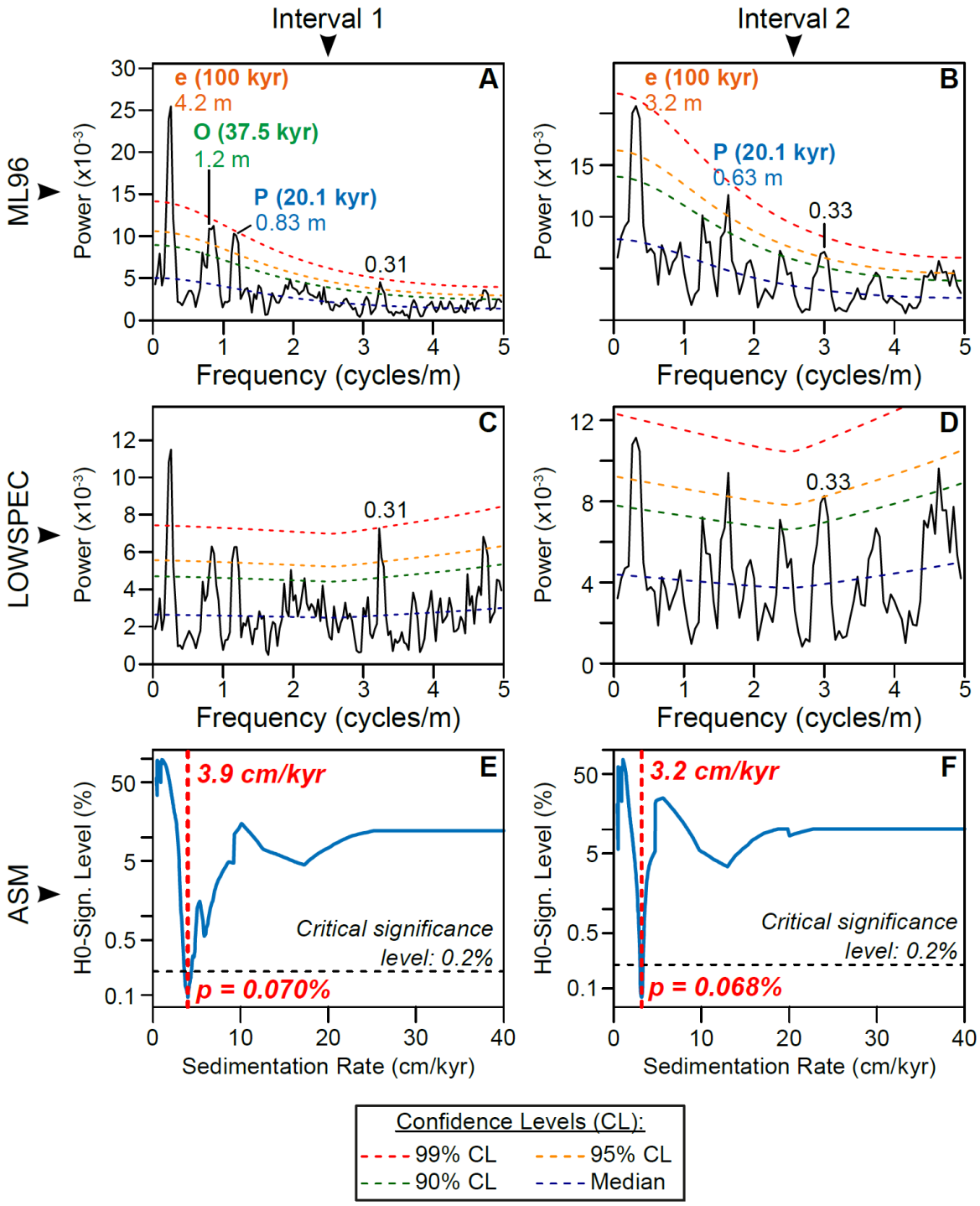

Fig. 5. 2π-MTM spectra and ASM results of the $\delta^{13}C$ series. **A. and B.** Spectra of intervals 1 and 2 with confidence levels calculated with the Mann and Lees (1996) method (ML96) with a Tukey's endpoint rule (Meyers, 2014). **C. and D.** Spectra of intervals 1 and 2 with confidence levels calculated with the LOWSPEC method (Meyers, 2012). **E. and F.** H0 significance levels from the ASM applied on intervals 1 and 2. The red dashed line indicates the sedimentation rate for which the sedimentary frequencies fit the best with the orbital frequencies.

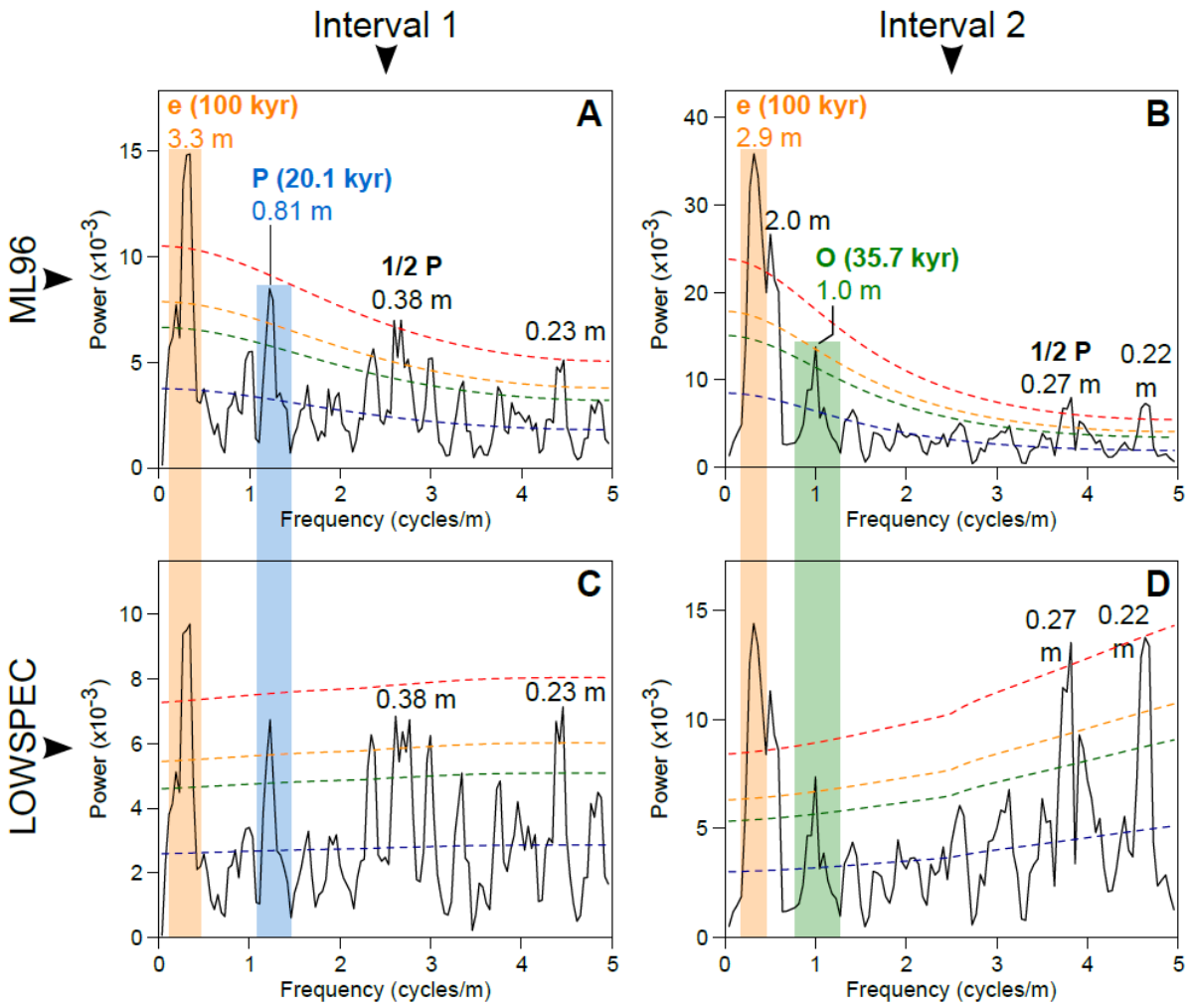

671

672 Fig. 6. 2π-MTM spectra of the magnetic susceptibility. **A. and B.** Spectra of intervals 1 and 2
673 with confidence levels calculated with the Mann and Lees (1996) method (ML96) with a
674 Tukey's endpoint rule (Meyers, 2014). **C. and D.** Spectra of intervals 1 and 2 with confidence
675 levels calculated with the LOWSPEC method (Meyers, 2012).

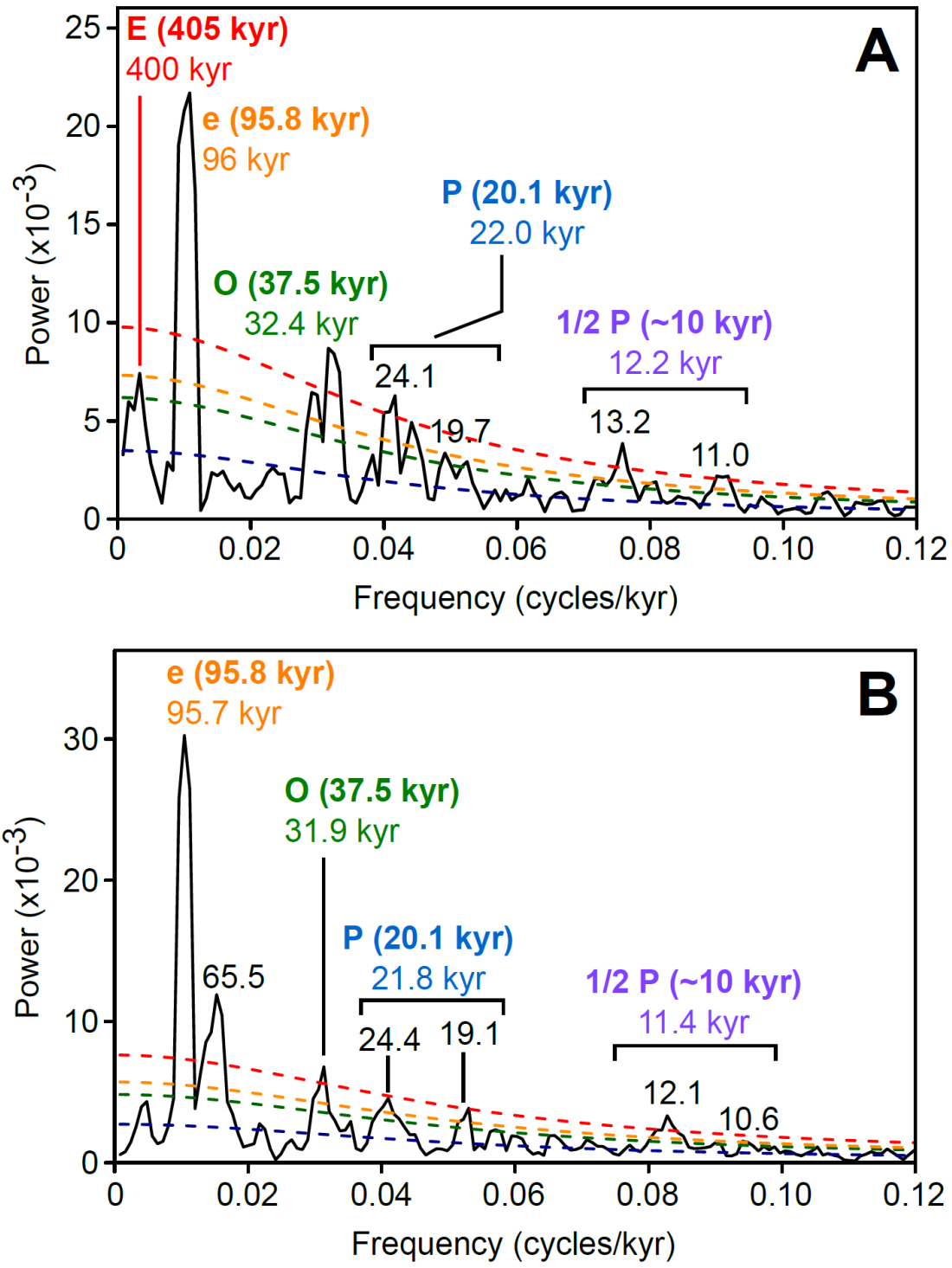

676

677 Fig. 7. 2π-MTM spectra of the (**A.**) calibrated $\delta^{13}C$ series, and (**B.**) calibrated MS series. The
678 main periods are labeled in kyr. The theoretical period of the corresponding astronomical cycle
679 is displayed in brackets. Abbreviations: E: 400-kyr eccentricity; e: 100-kyr eccentricity; O:
680 obliquity.

681

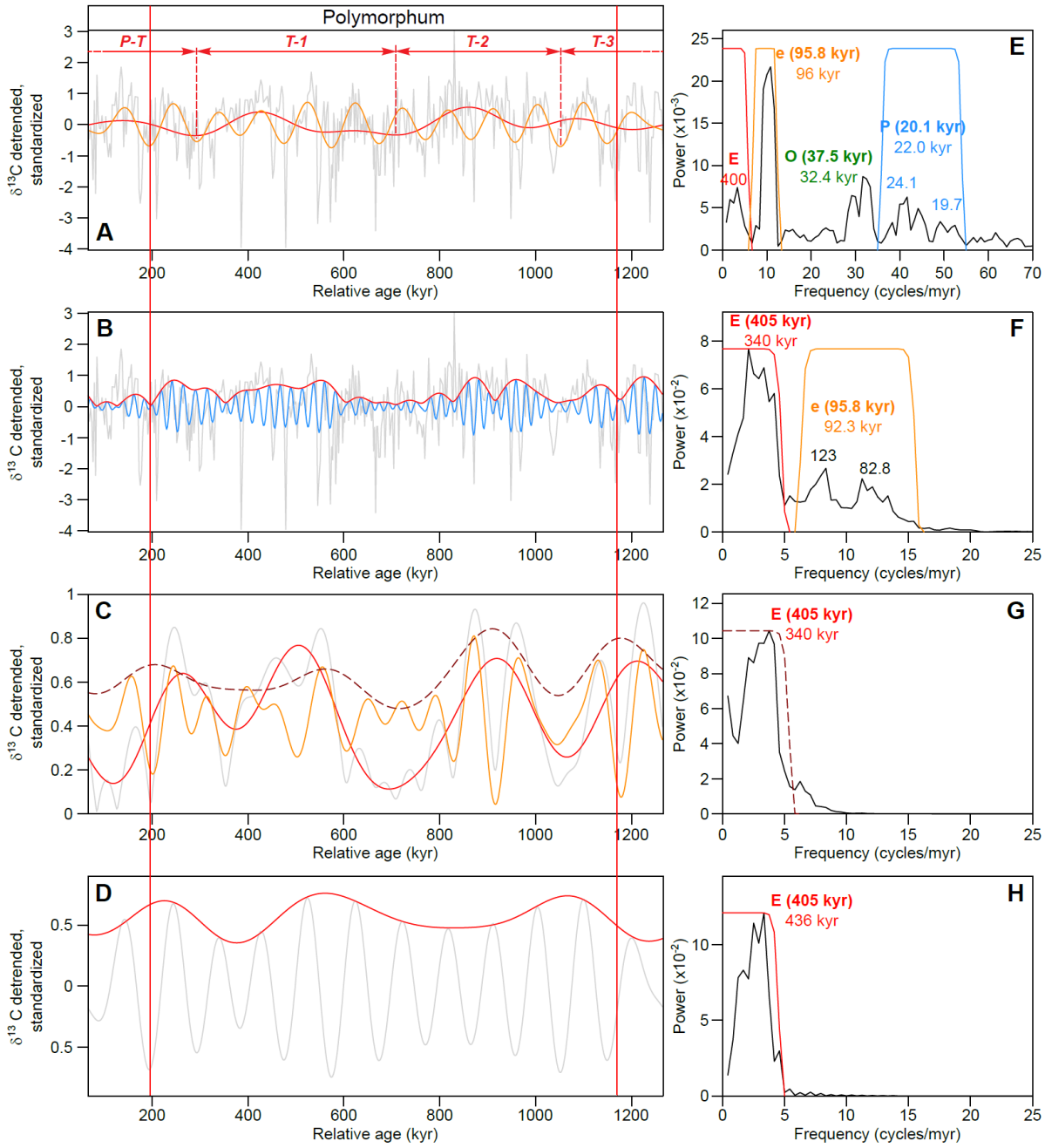

682

683 Fig. 8.

684

685

686

687

688

689 Fig. 8. Comparison between the direct filters of the eccentricity on the calibrated $\delta^{13}C$ signal
690 and the amplitude modulation of the precession in the calibrated $\delta^{13}C$. **A.** Filter of the 405-kyr
691 eccentricity (in red) and the 100-kyr eccentricity (in orange) of the calibrated $\delta^{13}C$ signal (in
692 grey). **B.** Filter of the precession (in blue) and its amplitude modulation (in red) of the calibrate
693 $\delta^{13}C$ signal (in grey). **C.** Filter of the 100-kyr cycle (in orange) and the 405-kyr cycle (in red)
694 obtained from the amplitude modulation of the precession cycle (in grey). In dashed brown:
695 Filter of the 405-kyr cycle obtained from the 100-kyr band of the amplitude modulation of the
696 precession. **D.** Filter of the 405-kyr cycle obtained from the amplitude modulation of the direct
697 filter of the 100-kyr cycle (in grey). **E.** Spectrum of the calibrated $\delta^{13}C$ series, with the filters
698 used for the 405-kyr cycle (in red; frequency cut: 0.005833 cycles/kyr; roll-off rate: 10^{36}), the
699 100-kyr cycle (in orange; frequency cuts: 0.006667 – 0.01250 cycles/kyr; roll-off rate: 10^{36})
700 and the precession cycle (in blue; frequency cuts: 0.03583 – 0.05417 cycles/kyr; roll-off rate:
701 10^{36}). **F.** 2π-MTM spectrum of the amplitude modulation of the precession cycles. The red and
702 orange curves represent the filter of the 405-kyr and 100-kyr eccentricity, respectively. The
703 405-kyr cycle is filtered with a Taner low-pass filter (frequency cut: 0.004833 cycles/kyr; roll-
704 off rate: 10^{36}). The 100-kyr cycle is filtered with a Taner band-pass filter (frequency cuts:
705 0.006250 – 0.01558 cycles/kyr; roll-off rate: 10^{36}). **G.** 2π-MTM spectrum of the amplitude
706 modulation of the 100-kyr cycle filtered from the amplitude modulation of the precession
707 cycles. The 405-kyr cycle (in red) is filtered using a Taner low-pass filter (frequency cut:
708 0.005417 cycles/kyr; roll-off rate: 10^{36}). **H.** 2π-MTM spectrum of the amplitude modulation of
709 the 100-kyr cycle filtered from the calibrated series. The 405-kyr cycle (in red) is filtered using
710 a Taner low-pass filter (frequency cut: 0.004583 cycles/kyr; roll-off rate: 10^{36}). Note that
711 spectra of panels F to H are obtained with a padding factor of 2.
712

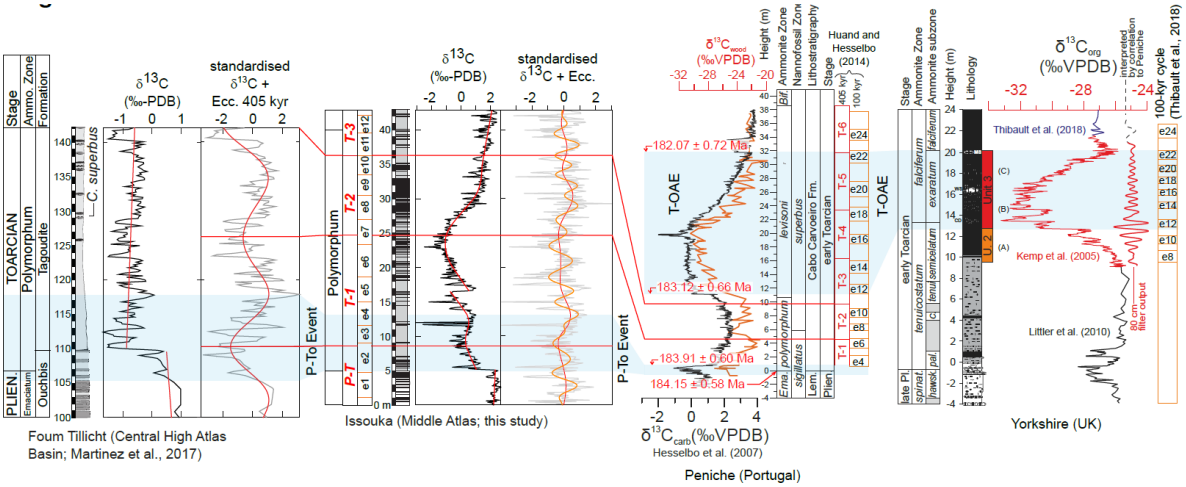

713

714 Fig. 9. Correlations of astronomical time scales in between the Central High Atlas Basin

715 (Martinez et al., 2017), the Middle Atlas Basin (present study), the Peniche section (Suan et

716 al., 2008b; Huang and Hesselbo, 2014) and the Yorkshire area (Thibault et al., 2018).